Porphyrin Interactions with Wild Type and Mutant Mouse Ferrochelatase

Ricardo Franco,[1†] Jian-Guo Ma,[2] Yi Lu,[2] Gloria C. Ferreira,[1] John A. Shelnutt[2]

[1]Department of Biochemistry and Molecular Biology, College of Medicine; Institute for Biomolecular Science; H. Lee Moffit Cancer Center and Research Institute, University of South Florida, Tampa, FL 33612.

[2]New Materials Theory and Validation Department, Sandia National Laboratories, Albuquerque 87185-1349 and Department of Chemistry, University of New Mexico, Albuquerque, NM 87131.

[†]Present Address: Departamento de Química, Faculdade de Ciências e Tecnologia, Universidade Nova de Lisboa, 2825 Monte de Caparica, Portugal

For submission to: *Biochemistry*

May 4, 1999

Sandia is a multiprogram laboratory operated by Sandia Corporation, a Lockheed Martin Company, for the United States Department of Energy under Contract DE-AC04-94-AL85000.

ABSTRACT

Ferrochelatase (EC 4.99.1.1), the terminal enzyme of the heme biosynthetic pathway, catalyzes Fe^{2+} chelation into protoporphyrin IX. Resonance Raman and UV-visible absorbance spectroscopies of wild type and engineered variants of murine ferrochelatase were used to examine the proposed structural mechanism for iron insertion into protoporphyrin by ferrochelatase. The recombinant variants (*i.e.*, H207N and E287Q) are enzymes in which the conserved amino acids histidine-207 and glutamate-287 of murine ferrochelatase were substituted with asparagine and glutamine, respectively. Both of these residues are at the active site of the enzyme as deduced from the *Bacillus subtilis* ferrochelatase three-dimensional structure. Addition of free base or metalated porphyrins to wild type ferrochelatase and H207N variant yields a quasi 1:1 complex, possibly a monomeric protein-bound species. In contrast, the addition of porphyrin (either free base or metalated) to E287Q is sub-stoichiometric, as this variant retains bound porphyrin in the active site during isolation and purification. The specificity of porphyrin binding is confirmed by the narrowing of the structure-sensitive resonance Raman lines and the vinyl vibrational mode. Resonance Raman spectra of free base and metalated porphyrins bound to the wild type ferrochelatase indicate a nonplanar distortion of the porphyrin macrocycle, although the magnitude of the distortion cannot be determined without first defining the specific type of deformation. Significantly, the extent of the nonplanar distortion varies in the case of H207N- and E287Q-bound porphyrins. In fact, resonance Raman spectral decomposition indicates a homogeneous ruffled distortion for the nickel protoporphyrin bound to the wild type ferrochelatase, whereas both a planar and ruffled conformations are present for the H207N-bound porphyrin. Perhaps more revealing is the unusual resonance

Raman spectrum of the endogenous E287Q-bound porphyrin, which has the structure-sensitive lines greatly upshifted relative to those of the free base protoporphyrin in solution. This could be interpreted as an equilibrium between protein conformers, one of which favors a highly distorted porphyrin macrocycle. Taken together these findings suggest that the mode of porphyrin distortion in murine ferrochelatase is different from that reported for yeast ferrochelatase, which requires metal binding for porphyrin distortion.

INTRODUCTION

The last step in the biosynthesis of heme is the insertion of ferrous iron into the protoporphyrin IX macrocycle. This reaction is catalyzed by ferrochelatase (protoheme ferrolyase, EC 4.99.1.1) {Ferreira et al., 1995; Dailey, 1996}. The eukaryotic enzyme is located in the matrix side of the inner mitochondrial membrane (*1*) {Dailey, 1990}. Ferrochelatase genes and cDNAs have been obtained and sequenced from many sources such as: bacteria (*2-4*), yeast (*5*), plants (*6*), frog (*7*), mouse (*8, 9*), bovine (*10*), and human {Nakahigashi et al., 1990}. With the development of heterologous overexpression systems, site-directed variants of ferrochelatase can be engineered and overproduced for investigation of the role of specific amino acids in the ferrochelatase reaction mechanism.

The X-ray crystal structure of the *Bacillus subtilis* enzyme has been solved to 1.9-Å resolution (*11*). The structure shows a cleft in a region containing several conserved amino acid residues proposed to be at the active site. Among these residues are a histidine (H183 in *B. subtilis* ferrochelatase and H207 in the murine mature enzyme) and a glutamate (E264 in *B. subtilis* ferrochelatase and E287 in the murine mature enzyme). The active site histidine and glutamate have been advocated to be involved in metal substrate binding(*12, 13*) and in catalysis (*14*), respectively. Biophysical characterization of human and mouse ferrochelatase has shown that these enzymes contain a [2Fe-2S] cluster (*15, 16*). In contrast, the bacterial, yeast and plant ferrochelatases have no known metal cofactors (*17*).

The proposed mechanism of ferrochelatase involves the distortion of the free base

protoporphyrin when bound to the active site cleft. This out-of-plane distortion exposes the pyrrole nitrogens to the metal atom promoting the insertion reaction. Evidence for this structural mechanism comes primarily from the strong inhibition of ferrochelatase by N-alkyl porphyrins, which exhibit such a nonplanar distortion (*18*). Indeed, *N*-methylporphyrins have been advocated to be transition state analogs for porphyrin metallation (*19*). Moreover, an antibody raised against a distorted porphyrin, *N*-methyl mesoporphyrin, catalyzed metal insertion into the porphyrin ring (*19, 20*), reinforcing the proposal that distortion of the porphyrin ring is one of the steps of the ferrochelatase catalytic mechanism. Recently, Blackwood *et al.*(*21*) reported that the catalytic antibody had a different mode of porphyrin binding than that of yeast ferrochelatase. In contrast to the catalytic antibody, the yeast ferrochelatase, an enzyme devoid of a [2Fe-2S] cluster, strained the porphyrin ring conformation with a tilting of all four pyrrole rings in the same direction ('doming'). However, this 'doming' distortion could only be detected upon the binding of Hg^{2+} (*21*) claimed to be a potent inhibitor of ferrochelatase activity (*18*).

In this study, we have used resonance Raman spectroscopy and other spectroscopic and biochemical techniques to investigate the mode of porphyrin interaction with murine wild type ferrochelatase and two site-directed mutants. Resonance Raman and UV-visible absorption spectra of various metal and free-base porphyrins bound to the wild type and engineered variants of murine ferrochelatase indicate a nonplanar distortion of the porphyrin macrocycle. Moreover, the degree of the nonplanar ring distortion was dependent on the mutations introduced in the active site of the enzyme. The resonance Raman spectroscopic results on the nonplanar distortion of the murine ferrochelatase-bound porphyrin are in contrast with those previously reported on the mode of interaction between free base porphyrin and yeast ferrochelatase. The

yeast enzyme-bound porphyrin displayed only significant macrocycle distortion when Hg^{2+} was also bound to the enzyme. Molecular mechanics calculations of porphyrin bound to the active site cleft of the *B. subtilis* ferrochelatase have also been used to further elucidate the proposed mechanism.

MATERIALS AND METHODS

Materials. Oligonucleotide primers were synthesized by Cybersyn, Inc., Lenni, PA and GIBCO BRL. Chameleon™ double-stranded, site-directed mutagenesis kit was a product from Stratagene. Sequenase and sequencing kit were from U.S. Biochemical Corp. [α-^{35}S]-dATP was from Dupont/NEN Research Products. Acrylamide and gel reagents were purchased from BioRad. The bicinchoninic acid protein assay reagents were obtained from Pierce Chemical Co.. Ni-NTA agarose and the QIAquick PCR purification kit were purchased from QIAGEN. All of the porphyrins used in these studies were from Porphyrin Products (Logan, UT). All other chemicals were of the highest purity available.

Construction of His-tagged H207N Ferrochelatase Plasmid. Plasmid pAP1, which contains the murine H207N ferrochelatase mutant cDNA sequence under the control of the alkaline phosphatase promoter, was constructed as previously described for plasmid pAP4 encoding the E287Q mutant {Franco et al., manuscript in preparation}. The mutagenic oligonucleotide for H207N was 5'-CTG TTT TCT GCC AAC TCC CTG CCG -3' (mutagenized base is in bold). Clones obtained after the mutagenesis procedure were screened using DNA sequencing according to the dideoxynucleotide chain termination method.{Sanger et al., 1977} The

resulting expression plasmid containing the mutation E287Q was named pAP4. To construct pGF57, an expression plasmid encoding the histidine-tagged H207N ferrochelatase mutant, pAP1 was digested with *Bsp*120 I and *Bam*H I, and the H207N mutation-containing DNA fragment was ligated into pGF47 {Franco et al., manuscript in preparation} previously treated with *Bsp*120 I and *Bam*H I.

Enzyme Preparation. Recombinant murine liver ferrochelatase was isolated and purified from hyperproducing DH5α *E. coli* cells containing the ferrochelatase expression plasmid pGF47. The mutant forms of ferrochelatase (E287Q and H207N) were isolated from hyperproducing DH5α *E. coli* cells harboring the corresponding mutated ferrochelatase expression plasmids. The purification scheme for the overproduced wild-type and mutant ferrochelatases has been described elsewhere {Franco *et al.*, in preparation}. The purified, concentrated proteins (typically 200 μM) in buffer H (20 mM Tris-HCl, pH 8, 10% glycerol, and 0.5 M NaCl) were frozen and stored in liquid nitrogen until use.

Porphyrin solutions. Porphyrin solutions were prepared by dissolving the appropriate amount of powder reagent in 0.1 N KOH (final pH=13). Stock porphyrin solutions for preparing the Raman and UV-visible absorption samples were typically about 2 mM.

Raman Samples. Raman samples were prepared in buffer H. The appropriate volumes of the respective stocks of porphyrin and ferrochelatase were added for a final volume of 500 μl and a porphyrin concentration of approximately 70 μM. The samples, contained in a stoppered 3x3 mm cross section optical cell (NSG Precision Cells), were incubated for 30 minutes under a

nitrogen flow in order to lower the oxygen concentration.

Resonance Raman spectra were obtained using the 406.7-nm line of an INNOVA Kr^+ laser (Coherent). The spectrometer was a 0.75-m monochromator (Instruments, SA) with a 512x2048 pixel LN_2-cooled CCD detector. The slit width of 100 μm for the 2400 groove/mm holographic grating gives a spectral resolution of 2 cm^{-1}. The CCD array was cooled by LN_2 to 138° K in a 2.8-L dewer controlled by the CCD3000 controller unit (Instruments, SA). The columns of the CCD chip (EEV) were binned to give 2048 13.5-μm channels or 0.3-cm^{-1} per channel. The chip is back-illuminated and has visible/NIR antireflection coatings. The spectrometer was interfaced to a 400-MHz Pentium II-based personal computer via an IEEE 488.2 PCI-GPIB interface card (National Instruments), and SpectraMax for Windows software (Instruments, SA) was used to collect the data from the CCD and control the spectrometer. Position mode was used for CCD region-mode detection covering about 500 cm^{-1} of the Raman spectrum. The spectra typically were obtained at room temperature in 3-10 minutes using 10-20 mW of laser power. Spectra were output as even-X ASCII files for plotting with *SigmaPlot* (SPSS).

UV-visible absorption spectral titrations. The titrations of the UV-visible absorption spectra were performed by adding increasing amounts of the respective porphyrin solution made in 0.1N KOH to a 10 μM protein in buffer H. The final volume of porphyrin solution added was always less than 5% of the total volume, and the pH of the reaction mixture was maintained at 8.0. UV-visible absorption spectra were recorded on a HP9852A diode array spectrophotometer. Acquired spectra were exported as ASCII files and imported into the graphing program *SigmaPlot* for presentation.

Ferrochelatase Activity Determinations. Enzymatic activity was determined using a modification of the continuous spectrofluorimetric assay (*22*). Briefly, ferrochelatase activity was monitored by following the rate of consumption of the free base mesoporphyrin IX [H_2(MesoP)] substrate. Kinetic measurements were conducted using a model RSM-1000F spectrofluorometer equipped with a temperature-controlled cell-holder and magnetic stirrer (OLIS, Inc.). The maximum excitation and emission wavelengths for mesoporphyrin IX under the assay conditions were 410 and 620 nm, respectively. The final concentrations of the substrates and enzyme in the reaction mixture were 2 μM for mesoporphyrin, 2 μM for Ni^{2+} and 30 nM for ferrochelatase. The reaction was initiated with addition of the metal substrate and was performed at 30 ^{0}C.

Molecular Mechanics Calculations. The influence of the active site of B. subtilis ferrochelatase on the shape of the macrocycle of nickel protoporphyrin IX was investigated using a modified(*23*) DREIDING II(*24*) force field containing atom types specific for Ni porphyrins. The force field has been developed and refined over the last decade and most recently described by Song *et al.*(*23*) and validated for many Ni porphyrin systems (*25-32*). The calculations were done by docking Ni(ProtoP) in the ferrochelatase cleft and then minimizing the Ni porphyrin with the atoms of the protein held fixed. Water molecules in the active site were also allowed to move. Several orientations of Ni(ProtoP) were used as initial structures for determining the variability of the macrocyclic structure imposed by the protein. Normal-coordinate structural decomposition (NSD)(*33-35*) was used to characterize the structure of the macrocycle. Structures were energy optimized to a force of 0.001 kcal/mole-Å without allowing the partial

charges on the porphyrin or protein to change during minimization and an *r*-dependent dielectric constant of 79 was used. Atomic charges for the Ni porphyrin were obtained by the charge equilibration method (*36*).

RESULTS

Nickel porphyrin complexes with mutant and wild type ferrochelatase

The resonance Raman spectra of wild type and mutant ferrochelatase and the complexes with various free base and nickel porphyrin derivatives are given in Figures 1, 2, 4, and 5 and the frequencies are listed in Tables 2 and 3.. Several spectra of solutions of the porphyrins are also given for comparison. Representative ultraviolet-visible absorption spectra showing the changes occurring upon addition of exogenous porphyrin are given in Figure 3. The relevance of the use of nickel porphyrin derivatives in this study was assessed by determining the enzymatic activity with Ni^{2+} and mesoporphyrin IX as substrates in the ferrochelatase-catalyzed reaction. Triplicate determinations of the enzymatic activity indicated a value of about 5% of that obtained with Zn^{2+} and mesoporphyrin as substrates, suggesting that nickel mesoporphyrin can be a product of the metallation reaction by ferrochelatase.

Ni(MesoP)-ferrochelatase complexes. UV-visible absorption spectral changes observed upon adding nickel mesoporphyrin [Ni(MesoP)] to wild type ferrochelatase, indicate binding of the porphyrin to the protein. Ni(MesoP) in solution at pH 8 shows a broad and blue-shifted Soret band. Upon addition of one equivalent of Ni(MesoP) to a ferrochelatase solution at pH 8, the Soret band red shifts and narrows probably indicating a monomeric species (Table 1). Adding extra equivalents (5) of nickel mesoporphyrin gives a mixture of the two spectra (data not shown).

The resonance Raman spectra of ferrochelatase with nickel mesoporphyrin [Ni(MesoP)] bound

are shown in Figure 1 along with monomeric Ni(MesoP) in CTAB for comparison. The frequencies obtained from Lorentzian decomposition of the Raman spectra are listed in Table 2. The Raman spectrum Ni(MesoP) in CTAB micelles at pH 8 (Figure 1A) is almost identical to the spectra of other nickel porphyrins such as nickel protoporphyrin IX [Ni(ProtoP)],(*37*) uroporphyrin [Ni(UroP)] (*37*), and octaethylporphyrin [Ni(OEP)] (*38*). All of these nickel porphyrins in solution exhibit an equilibrium mixture of planar and ruffled conformers, generally with somewhat higher populations of the nonplanar conformer based on the intensities of the two sublines making up the line shape of ν_{10}. The relative concentrations of these conformers is only slightly influenced by aggregation and solvation effects (*37*).

Binding of Ni(MesoP) to wild type ferrochelatase is indicated in the Raman spectrum shown in Figure 1B by the narrowing of the structure-sensitive Raman lines including ν_4, ν_3, ν_2, and ν_{10}. The narrowing for ferrochelatase is particularly evident in ν_{10}, which decreases from approximately 20 cm^{-1} for Ni(MesoP) in buffered CTAB solution to 12.7 cm^{-1} in the protein bound form. The ν_{10} line typically shows the largest downshifts upon ruffling of the macrocycle, which brings about the broadest line width for the solution mixture of planar and ruffled Ni(MesoP) species. Another indication of the binding to ferrochelatase is the downshifts in the peak frequencies of all of the structure-sensitive lines. The downshift is larger as the frequency of the marker line increases—the typical pattern of downshifts in the structure-sensitive lines when ruffling is the cause (*37-39*). For example, the downshifts of the nonplanar form for the CTAB solution are 4.9, 7.1 and 7.8 cm^{-1} for ν_3, ν_2, and ν_{10}, respectively. For protein-bound Ni(MesoP), both the narrowings and downshifts are a consequence of the disappearance of the mixture of conformers that occurs upon formation of a homogeneous ferrochelatase-bound

conformer. This bound Ni(MesoP) species is moderately more ruffled than the nearly planar conformer found in the solution studies, but not as ruffled as the solution ruffled conformer based on the size of the downshifts. From Lorentzian decomposition of the spectra in Figure 1, Ni(MesoP) in solution has ν_{10} at 1657.5 cm^{-1} for the planar conformer and at 1649.7 cm^{-1} for the ruffled conformer, a downshift of 7.8 cm^{-1} for the nonplanar conformer (Table 2). This is smaller than the approximately 20-cm^{-1} downshift observed for ruffled crystal structure of Ni(OEP) compared with the planar crystalline forms (*40*). The ruffling angle between the planes of the pyrrole rings is almost 33° for the ruffled Ni(OEP) crystalline form. The frequency of ν_{10} of the unique conformer of Ni(MesoP) bound to ferrochelatase is located at 1653.8 cm^{-1}, a downshift from the planar species frequency of only 3.7 cm^{-1}. This indicates a significant degree of ruffling (*vide infra*), while the narrowness of the line is consistent with a single homogeneous binding site. It is important to remember that the relationship between the Raman frequency and the ruffling deformation is nonlinear (Figure 8), with the dependence (slope) increasing as the ruffling increases. Thus, the ruffling may still be significant even for small downshifts in the structural marker lines.

Binding of Ni(MesoP) to the H207N ferrochelatase mutant results in a similar but larger change in the resonance Raman spectrum as shown in Figure 1C. A narrowing of the structure-sensitive lines is observed for the mutant, although the narrowing is not so dramatic as for the wild type. On the other hand, the decrease in frequencies of the structure-sensitive lines is greater for the mutant. For example, ν_{10} downshifts to 1650.8 cm^{-1}, a decrease of 6.7 cm^{-1} from the near planar form of Ni(MesoP) in buffered CTAB solution. As for the wild type, the downshifts for the lines increase with the frequency of the particular Raman line and thus indicate substantial ruffling of

the macrocycle.

A new weak line appears at 1628 cm^{-1} for the H207N mutant with added Ni(MesoP). This vinyl mode is also present in the spectrum of H207N without added porphyrin, indicating a small amount of endogenous free base protoporphyrin [H_2(ProtoP)]. (See Table 2.)

For the E287Q mutant, there is no conclusive evidence of binding of Ni(MesoP) to the protein. Indeed, complete binding of one equivalent of Ni(MesoP) is not expected because about 15% of the binding sites are already occupied by H_2(ProtoP), which is strongly bound to the mutant ferrochelatase as isolated (Franco *et al.*, in preparation). The structure-sensitive line frequencies assigned to Ni(MesoP) are clearly evident in the Raman spectrum shown in Figure 1D, and they are not significantly shifted or narrowed from the CTAB solution values. Specifically, ν_{10} is as broad and the sublines have nearly the same frequency as in the pH 8 CTAB solution. However, spectral decomposition reveals that the intensity of the subline of the ruffled species at 1653.4 cm^{-1}, near the frequency of for wild type ferrochelatase, is much larger than for the planar subline at 1659.4 cm^{-1}. For Ni(MesoP) in solution, the intensities are more nearly equal. Thus, it appears that a good fraction of the one equivalent of added Ni(MesoP) binds to the protein.

The lines of endogenous H_2(ProtoP) in the spectrum of the E287Q mutant in the presence of 1:1 Ni(MesoP):protein also demonstrates that endogenous H_2(ProtoP) is not displaced by Ni(MesoP). The spectrum of H_2(ProtoP) when endogenously bound to the E287Q mutant (shown in Figure 5E) is different from the CTAB solution spectrum of H_2(ProtoP) (Figure 5A), especially in the relative intensities of the lines. The protein-bound H_2(ProtoP) Raman spectrum

does not change when Ni(MesoP) is added. This is most easily seen in the resolved vinyl mode at 1626.6 cm^{-1}. The vinyl mode is only a shoulder on ν_{10} in the H_2(ProtoP) solution spectrum.

Ni(ProtoP)-ferrochelatase complexes. UV-visible absorption spectral changes observed upon adding Ni(ProtoP) to wild type ferrochelatase, indicate binding of the porphyrin to the protein. Ni(ProtoP) in solution at pH 8 shows a broad and blue-shifted Soret band. Upon addition of one equivalent of Ni(ProtoP) to a ferrochelatase solution at pH 8, the Soret band red shifts and narrows probably indicating a monomeric species (Table 1). Adding extra equivalents (5) of nickel protoporphyrin gives a mixture of the two spectra (data not shown). The observed red shifts of the Soret absorbance maxima of nickel protoporphyrin upon binding of wild type or site-directed ferrochelatase variants are indicated in Table 1.

The complex between Ni(ProtoP) and ferrochelatase is spectroscopically similar to the complex with Ni(MesoP). The resonance Raman spectrum of Ni(ProtoP) in aqueous solution at pH 8 is shown in Figure 2A for the region of the structure-sensitive lines for comparison with Ni(ProtoP) bound to ferrochelatase. Just as for Ni(MesoP), formation of the 1:1 complex between Ni(ProtoP) and wild type ferrochelatase (Figure 2B) results in a narrowing of the lines. Specifically, for ν_{10}, the line narrows from 20 cm^{-1} in solution to 12.7 cm^{-1} because the solution mixture of planar and nonplanar forms disappears for the ferrochelatase complex. Further, the frequencies of the structure-sensitive lines also decrease, indicating that the planar and nonplanar solution forms coalesce to a conformation of moderate nonplanarity. The downshifts from planar Ni(ProtoP) at pH 8 are 0.4, 3.1, 4.0, and 4.2 cm^{-1} for ν_4, ν_3, ν_2, and ν_{10}, respectively. The downshifts relative to planar Ni(ProtoP) at pH 13 in the absence of CTAB are similar. The

downshifts show the monotonic decrease with the decreasing frequencies of the Raman marker lines expected for ruffling. Thus the spectral changes upon binding of Ni(ProtoP) to ferrochelatase are entirely consistent with those observed for Ni(MesoP) binding.

The vinyl substituents appear to be influenced by binding to ferrochelatase as well since the vinyl stretching mode near 1633 cm^{-1} is much stronger in the spectrum of Ni(ProtoP)-ferrochelatase complex than in the solution spectra. The apparent increase in intensity of the vinyl mode results from the line narrowing associated with the homogeneous macrocycle conformation and particular vinyl orientation dictated by the active site in the protein. Specifically, curve fitting gives the line width for Ni(ProtoP)-bound to ferrochelatase of 9.8 cm^{-1}, compared to 12.6 cm^{-1} in buffer and 12.2 and 11.2 cm^{-1} for the H207N and E287Q mutants, respectively. Clearly, the binding site of the wild type protein is more homogeneous with respect to the interaction between the vinyl groups and the protein.

One-to-one binding of Ni(ProtoP) to ferrochelatase was verified by Raman spectra of a solution containing three equivalents of Ni(ProtoP). These spectra (not shown) show broader lines with higher frequencies more characteristic of the spectra of Ni(ProtoP) in aqueous solution at pH 8. The vinyl Raman line also weakens as expected if most of the Ni(ProtoP) is unbound.

The one-to-one complex of Ni(ProtoP) with the H207N mutant also shows the same spectral changes as the Ni(MesoP) complex. In particular, the Raman spectrum in Figure 2C shows mostly larger downshifts in the structure-sensitive lines, just as did this mutant for the Ni(MesoP) complex. An exception is the vinyl-sensitive ν_2 line. This line actually upshifts

relative to the 1:1 wild type position, while the vinyl mode itself downshifts by 3 cm^{-1}. This suggests different vinyl group positions in the mutant, either because of the increased nonplanar distortion or because of a specific localized interaction between the protein and the vinyl group(s). The structure-sensitive lines are a bit broader for the mutant than for the wild type proteins, indicating increased heterogeneity in the binding site of the mutant.

The detailed results of the Lorentzian spectral decomposition for Ni(ProtoP) in solution and bound to ferrochelatase and the H207N mutant are given in Table 3 for ν_{10}. Both planar and ruffled sublines are indicated for Ni(ProtoP) in buffer and for the H207N mutant, but only a single homogeneous ruffled form is supported for wild type ferrochelatase.

Like the Ni(MesoP) case, there is little evidence of binding of Ni(ProtoP) to the E287Q mutant in the resonance Raman spectrum shown in Figure 2D. ν_{10} is as broad and has nearly the same frequency as in the pH 8 solution (Figure 2A). The other structure-sensitive lines also have frequencies that are almost identical or slightly higher than Ni(MesoP) in solution at pH 8. Again, the spectrum of the endogenous free base protoporphyrin bound to the mutant (Figure 5D) is not apparently altered by the addition of one equivalent of Ni(ProtoP). Thus, the Raman data for the E287Q mutant is completely consistent with neither Ni(ProtoP) nor Ni(MesoP) being able to displace free base bound at the active site. In addition, there is little evidence to support binding to the unoccupied sites. However, spectral decomposition actually suggest that if the porphyrin is bound the interaction with the protein shifts the equilibrium in favor of the planar species. This conclusion is based on increased frequencies of ν_4, ν_3, and ν_2, and the large relative intensity of the planar subline of ν_{10} (Table 2).

Free-base porphyrin complexes with mutant and wild type ferrochelatase

H_2(MesoP)-ferrochelatase complexes. UV-visible absorption spectral changes observed upon adding free base mesoporphyrin to wild type ferrochelatase, indicating binding of the porphyrin to the protein. H_2(MesoP) in solution at pH 8 shows a broad and blue-shifted Soret band (Figure 3, solid line). Upon addition of one equivalent of H_2(MesoP) to a ferrochelatase solution at pH 8, the Soret band red shifts and narrows probably indicating a monomeric species (Figure 3, dashed line). Adding extra equivalents (5) of mesoporphyrin gives a mixture of the two spectra (Figure 3, dash-dotted line). The observed red shift of the Soret absorbance maxima of H_2(MesoP) upon binding of wild type ferrochelatase are indicated in Table 1.

The Raman spectra of free base mesoporphyrin and the ferrochelatase-H_2(MesoP) complexes are shown in Figure 4. Whether compared to H_2(MesoP) in buffered CTAB or in 0.1 N KOH (not shown), the structure-sensitive lines are slightly shifted for wild type ferrochelatase with one equivalent of H_2(MesoP). (Table 2) Specifically, ν_3 and ν_{10} are downshifted for wild type and also possibly for the H207N mutant. This result is consistent with that for binding of Ni porphyrins to ferrochelatase. However, the frequency of ν_2 appears to be upshifted slightly. In contrast with the wild type and H207 mutant, addition of H_2(MesoP) to the E287Q mutant shows little evidence of similar binding of added porphyrin. This indicates that the endogenously bound porphyrin is not displaced and its Raman lines are evident. (Compare Figure 4D and Figure 5D.)

H_2(ProtoP)-ferrochelatase complexes. UV-visible absorption spectral changes observed upon adding free base protoporphyrin [H_2(ProtoP)] to wild type ferrochelatase, indicate binding of the porphyrin to the protein. H_2(ProtoP) in solution at pH 8 shows a broad and blue-shifted Soret band. Upon addition of one equivalent of H_2(ProtoP) to a ferrochelatase solution at pH 8, the Soret band red shifts and narrows probably indicating a monomeric species (Table 1). Adding extra equivalents (5) of free base protoporphyrin gives a mixture of the two spectra (data not shown).

In the case of wild type ferrochelatase, the Raman spectrum shows that there is a small residual amount of porphyrin bound to the protein as isolated. Figure 5B shows the Raman spectrum of ferrochelatase at pH 8; a weak porphyrin Raman spectrum is evident. However, this spectrum differs considerably from the spectrum of H_2(ProtoP) in CTAB micelles at pH 8 shown in Figure 5A.

Figure 5C also shows the spectrum of the wild type ferrochelatase, but with one equivalent of H_2(ProtoP) added. Although the spectrum differs from as-isolated ferrochelatase, it shows some evidence of a significant fraction of a minor species with a spectrum that is similar to that of the residually bound porphyrin species. This is particularly evident in the shoulder at about 1626 cm^{-1} and the slightly increased intensity near 1560 cm^{-1}.

Figure 5D shows the spectrum of the H207N mutant with one equivalent of H_2(ProtoP). The spectrum looks almost identical to that of the wild type protein with added H_2(ProtoP). Two significant differences are that H207N has a broader ν_4 and a weaker vinyl mode than does the

wild type protein.

The spectrum of endogenous free base bound to the E287Q mutant in Figure 5E appears to be a mixture of two forms—one has a spectrum similar to the residual H_2(ProtoP) bound to wild type ferrochelatase and the other species has a spectrum similar to H_2(ProtoP) in the CTAB solution. Specifically, intensity from the former species is evident at about 1627 and 1562 cm^{-1} superimposed on a spectrum that is close to that of the free base in CTAB solution (Figure 5A). Apparently, some of the porphyrin is likely bound in a manner similar to that that remains bound during ferrochelatase preparation (Figure 5B), while some of it is almost unaffected by binding and has a spectrum like that of H_2(ProtoP) in the hydrophobic environment of micelles. The environments do differ however, as can be seen especially in the lower frequency of the line at 1532.5 cm^{-1} for the E287Q mutant and at 1536.7 cm^{-1} for solution H_2(ProtoP).

Molecular simulations of Ni(ProtoP) binding to *B. subtilis* ferrochelatase

The resonance Raman data for Ni(ProtoP) bound to murine ferrochelatase can be interpreted in the clearest possible way, since it remains four-coordinate and has no pyrrole protons and nitrogen lone pairs that can interact with the protein like the free base. For these reasons, we chose to investigate binding of Ni(ProtoP) at the active site of the known X-ray structure of the *B. subtilis* protein. Our goal is to determine whether the distortion that occurs upon binding is consistent with that indicated by the shifts in the structure-sensitive Raman lines.

Figure 6 shows two representative Ni(ProtoP) structures obtained by energy-optimization within the cleft of the *B. subtilis* X-ray crystal structure, and the normal-coordinate structural decomposition analyses of these and other Ni(ProtoP) structures are illustrated in Figure 7. The two low energy locations shown have the propionate groups of the heme oriented toward the interior of FC (Figure 6A) and toward the exterior solvent (Figure 6B). Other initial locations of the porphyrin, mostly further into the cleft, give structures that have about the same total distortion (root-squares displacements of the 24 macrocyclic atoms from the mean plane), although significant deformations other than ruffling occur. The energies vary considerably, but it should be remembered that the protein in these calculations is not allowed to adjust to the presence of the porphyrin other than that the water molecules in the cavity can move. All energies are lower than that of the isolated Ni(ProtoP) ruffled form except for two. The energies are lower because of favorable (negative) van der Waals interactions with the protein.

DISCUSSION

The proposed mechanism for the ferrochelatase-catalyzed reaction postulates that ferrochelatase functions by forcing the porphyrin ring towards a distorted conformation in which the two pyrrole-nitrogen electrons are more accessible to the incoming metal ion substrate. One of the steps for understanding the ferrochelatase catalytic mechanism involves the determination of the nonplanar porphyrin distortion caused by ferrochelatase and the identification of the protein determinants responsible for the macrocyclic distortion. The work reported here investigates the mechanism of porphyrin binding to wild type and site-directed mutant forms of ferrochelatase and demonstrates that a modest nonplanar distortion of the macrocycle occurs upon binding. Furthermore, the results show that the magnitude of the distortion depends on mutation of amino acid residues involved in catalysis.

Titration of free base or nickel porphyrins into solutions of ferrochelatase clearly indicates specific one-to-one binding to the protein. This conclusion is based on both UV-visible absorption spectra and resonance Raman data as a function of porphyrin concentration. Presumably binding occurs at the active site since the E287Q mutant, which retains endogenous H_2(ProtoP) during isolation of the protein, does not unmistakably bind all of the added porphyrins in a specific manner. It is important to note that porphyrin solutions at a concentration required for the resonance Raman studies (*i.e.*, 70 μM) could not be reached by simply diluting the free-base porphyrin (prepared in 0.1 M KOH) in buffer H. In the absence of protein, these conditions were conducive to porphyrin aggregation. However, the porphyrin solutions of required concentration were easily obtained by direct dilution of the porphyrin (*i.e.*,

in 0.1 M KOH) in buffer H *containing ferrochelatase*. It is possible that the protein environment prevents porphyrin aggregation by providing a more hydrophobic environment, in a similar role to that of a detergent. Furthermore, porphyrin binding appears to be specific, *i.e.*, in the active site of wild type ferrochelatase.

The distortion of the porphyrin macrocycle that occurs might be thought to be small based on the small observed Raman shifts; however, this not necessarily the case. Studies of model nonplanar Ni porphyrins undergoing different types of deformation, *e.g.*, ruffling, doming, and saddling, indicate different sensitivities of the structure-sensitive Raman lines to the magnitude of the particular deformation. The ruffling deformation involves twisting of the pyrrole rings of the porphyrin about the metal-nitrogen bond, whereas saddling and doming involve tilting about an axis perpendicular to the metal-nitrogen bond.

From model compound studies,(*30, 32*) it is known that the marker lines are much more sensitive to ruffling than to saddling. This data is plotted for the first time in Figure 8 using NSD to determine the magnitudes of the *ruf* and *sad* deformations for the synthetic Ni porphyrins used in these studies. Depending on the particular structure-sensitive line, one estimates between 5.8 (ν_4) and 9.4 (ν_3) times higher frequency sensitivity to ruffling than to saddling, based on the *b* parameters determined from least-square fitting of the data in Figure 8. Thus, if the distortion is purely saddled the small frequency shifts that occur upon binding might indicate sizable saddling deformations. Another factor to be considered in evaluating the meaning of the observed shifts in the Raman lines is the nonlinear frequency dependence on distortion. That is, the frequency dependence on distortion (slope) is initially small but becomes stronger as the distortion

increases proportional to the third power of the deformation.

Although the magnitude and type of symmetric deformations making up the porphyrin distortion in ferrochelatase is still uncertain, it is clear from the resonance Raman data that some sort of distortion occurs and is different for the two mutant proteins. The distortion is evident from downshifts in the structure-sensitive line frequencies for both the free base and the nickel porphyrins and for both MesoP and ProtoP. Thus, it is clear that the active site prefers at least a moderately nonplanar macrocycle.

How large are the deformations in ferrochelatase? We can obtain a crude estimate of the deformations by assuming the downshift alternatively arise from a pure ruffling or pure saddling deformation and by using the relationships of Figure 8 to calculate the size of the deformation. It would be best to use the downshifts in ν_{10}, which are more accurate because of the higher sensitivity to deformation. However, ν_{10} is not observed in the model compound Raman data currently available. Instead, we use the downshifts in ν_3 to obtain an estimated of the extent of ruffling and saddling of ferrochelatase-bound porphyrin. For ruffling, using the 2.2-cm^{-1} downshift relative to the planar solution species, we obtain from $\Delta\nu_3 = \nu_3(0) - \nu_3(\delta) = -b\delta^4$, where $\Delta\nu_3 = 2.2$ cm^{-1}. Thus, the magnitude of the ruffling deformation for ferrochelatase is $\delta_{ruf} = (-\Delta\nu_3/b)^{1/4} =$ 1.3 Å. The larger downshift for the H207N mutant (3.5 cm^{-1}) gives a larger ruffling of 1.4 Å, and the smaller downshift for the E287Q mutant (0.4 cm^{-1}) give a 0.8 Å ruffling. If the shift is fully accounted for by saddling the deformation is large. From the same downshifts, the magnitude of the saddling is 2.6, 2.9, and 1.7 Å, respectively, for the wild type, H207N, and E287Q mutant proteins.

Clearly, the magnitude and possibly the relative contributions of the different types of symmetric deformations to the porphyrin distortion are altered by mutation of the conserved residues at the active site. For both Ni(MesoP) and Ni(ProtoP), binding to the H207N mutant causes larger decreases in frequency and presumably a larger distortion. However, the type of symmetric deformation affects the frequency dependence; thus, the frequency shifts could increase for the H207N mutant because the types of deformation making up the distortion change without significantly changing the total magnitude of distortion. This suggests that histidine-207 may be more directly involved in catalysis than just binding the iron atom. His-207 may influence macrocycle conformation as well. It is possible that the mutation has a simple steric effect and that the unfavorable positioning of the introduced asparagine residue would cause the larger distortion or change in shape.

The model calculations for the *B. subtilis* enzyme certainly suggest that the putative active site does not support a planar porphyrin. The structures obtained are mainly ruffled and ruffled to an extent consistent with our estimates of the ruffling based on the Raman downshifts associated with binding to the enzyme. From Figure 7, we see that the ruffling varies from 0.4 to 2.0 Å, and for the two low-energy structures shown in Figure 6 the ruffling is 1.3 and 1.5 Å. The calculated structure are thus consistent with the 1.3-Å ruffling calculated from the Raman downshifts.

The frequencies of the sublines for the H207N mutant suggest that the site is more heterogeneous since at least two conformers differing in the ruffling exist. In addition, the ruffling for the H207N mutant is still not as great as for the ruffled solution conformer but greater than for the

conformer in ferrochelatase. However, these conclusions are based on the assumption that ruffling causes the difference. Instead, large differences in other types of deformation might account for the frequency differences in marker lines.

For the E287Q mutant, the mutation has a large effect on the affinity for free base porphyrin. Specifically, free base porphyrin remains bound to about 15% of the mutant protein during preparation, much more than for wild type ferrochelatase. Furthermore, the porphyrin is not displaced by nickel porphyrins that bind to wild type with high enough affinity to give almost complete complex formation at one equivalent of added porphyrin (Figures 1D and 2D). Finally, the mode of binding to wild type and E287Q mutant differs, since the Raman spectra of the endogenously bound porphyrin of wild type and the E287Q mutant differ significantly (Figure 5, B and E).

The strong influence of the mutation of glutamic acid-287 (Figure 6A) suggests that it may play a part in the binding of the substrate to the enzyme. The unusual Raman spectrum of the endogenous porphyrin of ferrochelatase (Figure 5B) and its similarity to the E287Q spectrum (Figure 5E) suggest that free base porphyrin interacts strongly with the glutamic acid, giving a porphyrin species that is uniquely different from the solution models (*e.g.*, Figure 5A). From Figure 6B, it is clear that for some orientations of the substrate a propionate of the porphyrin could interact strongly with the neutral glutamine-287 of the mutant, but weakly with the negative glutamic acid residue of the wild type. Alternatively, it could be that if E287 has a direct catalytic role. The excess substrate-binding energy of the porphyrin that is used by the wild type protein to reduce the K_{cat} value *cannot* be used by the mutant since it cannot abstract

the pyrrole proton(s). In other words, this mutant is "stuck" during the catalytic process—it cannot release the product and thus has a much lower enzymatic activity. It is possible that the binding of the porphyrin is affected not because E287 is directly involved in porphyrin binding but because the catalytic process is hindered.

Ni(ProtoP) and probably H_2(ProtoP) show decreases in frequency of ν_2 that are probably indicative of a different specific orientation of the vinyl substituents for the wild type ferrochelatase complex. For Ni(ProtoP), this is consistent with the change in intensity and perhaps frequency of the vinyl mode near 1633 cm^{-1}.

We still do not have a definitive interpretation of the drastically altered spectrum of the endogenous porphyrin bound to wild type and E287Q ferrochelatase. The large shifts in frequency of the structure-sensitive lines, and apparent disappearance (wild type) or downshift (E287Q) of ν_2 could indicate a large distortion of the macrocycle. However, the observed upshifts in frequency of ν_4 and downshifts in ν_3 and ν_{10} would not be expected for a ruffled or saddled porphyrin. A specific interaction with the pyrrole protons might cause such frequency shifts. Clearly, a better understanding of the origin of these shifts might further elucidate the catalytic mechanism.

Currently, further resonance Raman studies of N-methylporphyrin binding to mouse ferrochelatase and its mutants are underway. We have not yet investigated effects of metal binding on the out-of-plane conformation of the porphyrins. Other authors (*21, 41*) have used Hg as a competitive inhibitor to freeze the substrate porphyrin in an activated-state conformation.

However, our own observations of Hg titrations of ferrochelatase followed by UV/visible and CD spectroscopies, indicate that the cluster is destroyed at Hg:protein ratios as low as 0.25 and that the protein starts getting irreversibly denatured at Hg:protein ratios of 1.0 (data not shown).

ACKNOWLEDGEMENTS

We thank the following institutions for funding: The American Cancer Society (Grant BE-248) and the National Institutes of Health (Grant DK51186) (to G.C.F.). Sandia is a multiprogram laboratory operated by Sandia Corporation, a Lockheed Martin Company, for the United States Department of Energy under Contract DE-AC04-94AL85000 (J.A.S.).

REFERENCES

1. Harbin, B. M., and Dailey, H. A. (1985) *Biochemistry 24*, 366-70.
2. Nakahigashi, K., Nishimura, K., Miyamoto, K., and Inokuchi, H. (1991) *Proc Natl Acad Sci USA 88*, 10520-4.
3. Frustaci, J. M., and O'Brian, M. R. (1992) *J Bacteriol 174*, 4223-9.
4. Kanazireva, E., and Biel, A. J. (1996) *Gene (Amsterdam) 170*, 149-150.
5. Labbe-Bois, R. (1990) *J Biol Chem 265*, 7278-83.
6. Miyamoto, K., Tanaka, R., Teramoto, H., Masuda, T., Tsuji, H., and Inokuchi, H. (1994) *Plant Physiol 105*, 769-70.
7. Day, A. L., Parsons, B. M., and Dailey, H. A. (1998) *Archives of Biochemistry and Biophysics 359*, 160-9.
8. Taketani, S., Nakahashi, Y., Osumi, T., and Tokunaga, R. (1990) *J Biol Chem 265*, 19377-80.
9. Brenner, D. A., and Frasier, F. (1991) *Proc Natl Acad Sci USA 88*, 849-53.
10. Shibuya, H., Nonneman, D., Tamassia, M., Allphin, O. L., and Johnson, G. S. (1995) *Biochim Biophys Acta 1231*, 117-20.
11. Al-Karadaghi, S., Hansson, M., Nikonov, S., Jonsson, B., and Hederstedt, L. (1997) *Structure (London) 5*, 1501-1510.
12. Kohno, H., Okuda, M., Furukawa, T., Tokunaga, R., and Taketani, S. (1994) *Biochim Biophys Acta 1209*, 95-100.
13. Franco, R., Moura, J. J. G., Moura, I., Lloyd, S. G., Huynh, B. H., Forbes, W. S., and Ferreira, G. C. (1995) *J Biol Chem 270*, 26352-26357.

14. Gora, M., Grzybowska, E., Rytka, J., and Labbe-Bois, R. (1996) *J Biol Chem 271*, 11810-11816.

15. Ferreira, G. C., Franco, R., Lloyd, S. G., Pereira, A. S., Moura, I., Moura, J. J. G., and Huynh, B. H. (1994) *J Biol Chem 269*, 7062-7065.

16. Dailey, H. A., Finnegan, M. G., and Johnson, M. K. (1994) *Biochemistry 33*, 403-407.

17. Ferreira, G. C., Franco, R., Lloyd, S. G., Moura, I., Moura, J. J. G., and Huynh, B. H. (1995) *Journal of Bioenergetics and Biomembranes 27*, 221-229.

18. Dailey, H. A., and Fleming, J. E. (1983) *J Biol Chem 258*, 11453-9.

19. Cochran, A. G., and Schultz, P. G. (1990) *Science 249*, 781-783.

20. Romesberg, F. E., Santarsiero, B. D., Spiller, B., Yin, J., Barnes, D., Schultz, P. G., and Stevens, R. C. (1998) *Biochemistry 37*, 14404-9.

21. Blackwood, M. E., Jr., Rush, T. S., III, Romesberg, F., Schultz, P. G., and Spiro, T. G. (1998) *Biochemistry 37*, 779-782.

22. Abbas, A., and Labbe-Bois, R. (1993) *J Biol Chem 268*, 8541-8546.

23. Song, X. Z., Jentzen, W., Jia, S. L., Jaquinod, L., Nurco, D. J., Medforth, C. J., Smith, K. M., and Shelnutt, J. A. (1996) *J Am Chem Soc 118*, 12975-12988.

24. Mayo, S. L., Olafson, B. D., and Goddard, W. A. (1990) *J Phys Chem 94*, 8897-8909.

25. Song, X. Z., Jaquinod, L., Jentzen, W., Nurco, D. J., Jia, S. L., Khoury, R. G., Ma, J. G., Medforth, C. J., Smith, K. M., and Shelnutt, J. A. (1998) *Inorg Chem 37*, 2009-2019.

26. Song, X. Z., Jentzen, W., Jaquinod, L., Khoury, R. G., Medforth, C. J., Jia, S. L., Ma, J. G., Smith, K. M., and Shelnutt, J. A. (1998) *Inorg Chem 37*, 2117-2128.

27. Sparks, L. D., Medforth, C. J., Park, M. S., Chamberlain, J. R., Ondrias, M. R., Senge, M. O., Smith, K. M., and Shelnutt, J. A. (1993) *J Am Chem Soc 115*, 581-592.

28. Sparks, L. D., Chamberlain, J. R., Hsu, P., Ondrias, M. R., Swanson, B. A., Demontellano, P. R. O., and Shelnutt, J. A. (1993) *Inorg Chem 32*, 3153-3161.

29. Sparks, L. D., Anderson, K. K., Medforth, C. J., Smith, K. M., and Shelnutt, J. A. (1994) *Inorg Chem 33*, 2297-2302.

30. Jentzen, W., Simpson, M. C., Hobbs, J. D., Song, X., Ema, T., Nelson, N. Y., Medforth, C. J., Smith, K. M., Veyrat, M., Mazzanti, M., Ramasseul, R., Marchon, J. C., Takeuchi, T., Goddard, W. A., III, and Shelnutt, J. A. (1995) *J Am Chem Soc 117*, 11085-11097.

31. Shelnutt, J. A., Majumder, S. A., Sparks, L. D., Hobbs, J. D., Medforth, C. J., Senge, M. O., Smith, K. M., Miura, M., Luo, L., and Quirke, J. M. E. (1992) *J Raman Spectrosc 23*, 523-529.

32. Shelnutt, J. A., Medforth, C. J., Berber, M. D., Barkigia, K. M., and Smith, K. M. (1991) *J Am Chem Soc 113*, 4077-4087.

33. Jentzen, W., Song, X., and Shelnutt, J. A. (1996) *Biophys J 70*, A153.

34. Jentzen, W., Ma, J. G., and Shelnutt, J. A. (1998) *Biophys J 74*, 753-63.

35. Shelnutt, J. A., Song, X. Z., Ma, J. G., Jia, S. L., Jentzen, W., and Medforth, C. J. (1998) *Chem Soc Rev 27*, 31-41.

36. Rappe, A. K., Goddard III, W. A. (1991) *J Phys Chem 95*, 3358-3363.

37. Alden, R. G., Ondrias, M. R., and Shelnutt, J. A. (1990) *J Am Chem Soc 112*, 691-697.

38. Alden, R. G., Crawford, B. A., Doolen, R., Ondrias, M. R., and Shelnutt, J. A. (1989) *J Am Chem Soc 111*, 2070-2072.

39. Anderson, K. K., Hobbs, J. D., Luo, L., Stanley, K. D., Quirke, J. M. E., and Shelnutt, J. A. (1993) *J Am Chem Soc 115*, 12346-12352.

40. Brennan, T. D., Scheidt, W. R., and Shelnutt, J. A. (1988) *J Am Chem Soc 110*, 3919-

3924.

41. Blackwood, M. E., Rush, T. S., Medlock, A., Dailey, H. A., and Spiro, T. G. (1997) *J Am Chem Soc 119*, 12170-12174.

Table 1. Shifts in Porphyrin Soret Bands upon Binding to Wild Type and Mutant Ferrochelatase

Porphyrin[1]	Protein	Free Porphyrin, Soret band (nm)	Protein-bound porphyrin,[2] Soret band (nm)	Soret band shift(nm)
H_2(MesoP)	Wild type	372	400	**28**
Ni(MesoP)	Wild type	380	394	**14**
H_2(ProtoP)*	Wild type	400	413	**13**
Ni(ProtoP)	Wild type	382	402	**20**
Ni(ProtoP)	H207N	382	384	**2**
Ni(ProtoP)	E287Q	382	390	**8**

[1]Porphyrin stock solutions were made in 0.1 M KOH, pH=13, except for that of H_2(ProtoP), which is denoted with an asterisk. The H_2(ProtoP) was made in water containing 0.4% Triton X-100 and 4 mM NH_4OH. Porphyrins were diluted in buffer H or in buffer H containing 10 μM protein to a final concentration of 10 μM and pH ~ 8.2.

[2]Porphyrins were added to ferrochelatase (wild type or mutants) in buffer H at a molar ratio of 1:1.

Table 2. **Frequencies (cm^{-1}) of some of the Raman lines in the 1300 to 1700 cm^{-1} region obtained from Lorentzian decomposition of the spectra of ferrochelatase and the H207N and E287Q mutants with and without bound Ni(MesoP), Ni(ProtoP), H_2(ProtoP), and H_2(MesoP).**

	ν_4	ν_3, np	ν_3, p	ν_2, np	ν_2, p			ν_{10}, np	ν_{10}, p	ν_{vinyl}
Ni(MesoP)										
CTAB	1378.7	1515.9	1520.8	1597.9	1605.0			1649.7	1657.5	
FC	1378.7	1518.6		1603.0				1653.8		
H207N	1377.9	1517.3		1595.4	1602.2			1650.8		
						(1560.6)				(1627.5)
E287Q	1380.3	1520.4		1604.0				**1653.4**[a]	1659.4	
	(1365.4)[b]	(1476.9)		(1534.0)		(1561.3)	(1580.0)			(1626.6)
Ni(ProtoP)										
CTAB	1380.0	1517.2	1522.2	1595.9				**1654.9**	1660.3	1632.6
FC	1379.6	1519.1		1591.9				1656.1		1633.7
H207N	1378.2	**1516.5**	1521.2	1593.3				**1652.0**	1659.1	1630.8

E287Q	1382.5		1522.2	1596.7			1652.6	**1659.6**	1630.9
	(1369.0)		(1480.8)	(1536.2)		(1563.4)	(1597.6)	(1615.8)	?
H_2(ProtoP)									
CTAB	1360.0	1368.1	1478.9	1536.7		1561.6	1584.1	1614.3	1626.3
FC	1356.4	**1366.6**	1477.9	1530.4	1537.8	1560.7	1584.6	1613.6	1626.0
H207N	1355.5	**1365.0**	1478.2	1536.8		1561.7	1583.1	1612.0	1626.8
H_2(MesoP)									
CTAB	1356.9	**1364.0**	1479.7	1544.3		1566.7	1587.8	1613.2	
FC	1364.5		1478.9	1544.9		1557.1	1582.5	1612.1	
H207N	1364.4		1479.3	1546.5		1563.0	?	1613.6	
E287Q	1362.0		1478.8	1546.5		1561.4	1586.4	1614.0	
	(1366.6)			(1533.5)					(1627.2)
FC	1370.3					1563.3	1588.9	1608.6	1626.5
H207N	1368.3					1570.5	H_2O?	1609.5	1628.7
E287Q	1365.4		1478.1	1532.5		1561.8	1583.8	1610.9	1627.0

[a]The frequency is in bold type for the subline that overwhelmingly dominates. [b]Lines assigned to endogenous porphyrin.

Table 3. Spectral decomposition of ν_{10} of nickel protoporphyrin bound to ferrochelatase, the H207N mutant, and in solution.

Raman Line	Frequency (cm^{-1})	Width (cm^{-1})	Area ratio, np:p
buffer H			
ν_{10}, nonplanar	1654.9±0.4	22.9±0.6	5.3
ν_{10}, planar	1660.3±0.2	8.1±0.8	
1:1 FC			
ν_{10}, nonplanar	1656.1±0.1	12.8±0.1	>10
1:1 H207N			
ν_{10}, nonplanar	1652.0±0.4	14.3±0.7	2.6
ν_{10}, planar	1659.1±0.4	10.8±1.1	

FIGURE CAPTIONS

Figure 1. Resonance Raman spectra of nickel mesoporphyrin IX [Ni(MesoP)] bound to wild type and mutant ferrochelatase in pH 8 buffer. (A) Ni(MesoP) in CTAB micellar solution; (B) wild type ferrochelatase plus one equivalent of Ni(MesoP); (C) H207N mutant ferrochelatase plus one equivalent of Ni(MesoP); and (D) E287Q mutant plus one equivalent of Ni(MesoP). Light excitation is at 406.7 nm using a Kr^+ laser.

Figure 2. Resonance Raman spectra of nickel protoporphyrin IX [Ni(ProtoP)] bound to wild type and mutant ferrochelatase in pH 8 buffer. (A) Ni(ProtoP) in buffered solution; (B) wild type ferrochelatase plus one equivalent of Ni(ProtoP); (C) H207N mutant ferrochelatase plus one equivalent of Ni(ProtoP); and (D) E287Q mutant plus one equivalent Ni(ProtoP). Light excitation is at 406.7 nm using a Kr^+ laser.

Figure 3. UV-visible absorption spectrum of free base mesoporphyrin IX [H_2(MesoP)]. In solution (—) and bound to wild type ferrochelatase (FC) with H_2(MesoP)/FC (molar ratio) = 1 (– – –) and with H_2(MesoP)/FC (molar ratio) = 5 (-··-··-).

Figure 4. Resonance Raman spectra of free base mesoporphyrin IX [H_2(MesoP)] bound to wild type and mutant ferrochelatase. (A) H_2(MesoP) in pH 8 buffered CTAB solution; (B) wild type ferrochelatase plus one equivalent of H_2(MesoP) at pH 8; (C) H207N mutant with one equivalent of H_2(MesoP) at pH 8; and (D) E287Q mutant with one equivalent of H_2(MesoP) at pH 8.0. Light excitation is at 406.7 nm using a Kr^+ laser.

Figure 5. Resonance Raman spectra of free base protoporphyrin IX [H_2(ProtoP)] bound to wild type and mutant ferrochelatase in pH 8 buffer. (A) H_2(ProtoP) in buffered CTAB solution; (B) wild type ferrochelatase without added protoporphyrin; (C) wild type ferrochelatase plus one equivalent of H_2(ProtoP); (D) H207N ferrochelatase plus one

equivalent of H_2(ProtoP); and (E) E287Q mutant without added protoporphyrin. Light excitation is at 406.7 nm using a Kr^+ laser. Asterisk indicates lines of aqueous buffer H.

Figure 6. The active site of *B. subtilis* ferrochelatase showing the conformation of energy minimized Ni(ProtoP) (and water molecules, not shown) for two low energy structures, A: 44.7 kcal/mol; B: 49.4 kcal/mol.

Figure 7. NSD deformations of energy-optimized Ni(ProtoP) isolated (top) and located at seven different locations in the cleft of *B. subtilis* ferrochelatase. Water molecules in the cleft were movable in the simulations, but the protein and other waters were fixed at the X-ray structure coordinates. The total energies are given for each structure. The lowest energy structure (bottom) has the propionates oriented toward the interior of the protein, but the energy of the next lowest energy structure has the propionates oriented toward the solvent. The high-energy structures are generally located deeper in the crevice.

Figure 8. Relationships between Raman frequency and magnitude of deformation for series of predominantly ruffled (*ruf*) nickel porphyrins (Ni tetraalkyl(aryl)porphyrins)(*30*) and predominantly saddled porphyrins (Ni octaalkyl-tetraphenylporphyrins) (*32*). The curves are least-squares fits using the functional form $\nu = a + b\delta^4$, where δ is the magnitude of the deformation in Ångstroms. The intercept at zero deformation, a, and b are the fitting parameters. The values for b for ν_4, ν_3, and ν_2 are given in the figure; those for a are 1374.3, 1480.3, 1575.1 cm^{-1} for ruffling and 1383.4, 1523.1, and 1595.2 cm^{-1} for saddling, respectively. ν_{10} was not observed.

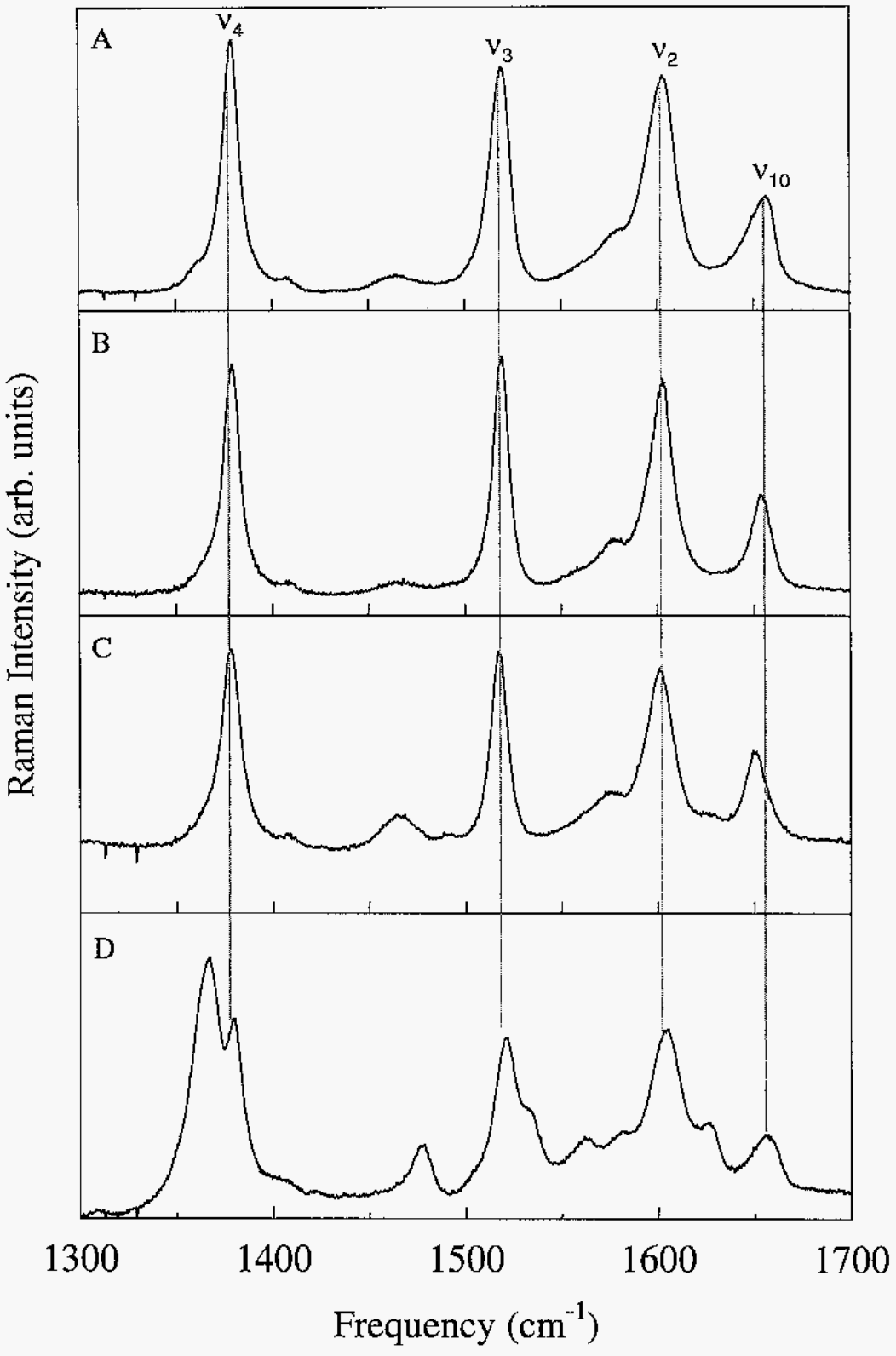
A
B
C
D
ν_4
ν_3
ν_2
ν_{10}
Raman Intensity (arb. units)
1300
1400
1500
1600
1700
Frequency (cm^{-1})

Figure 1.

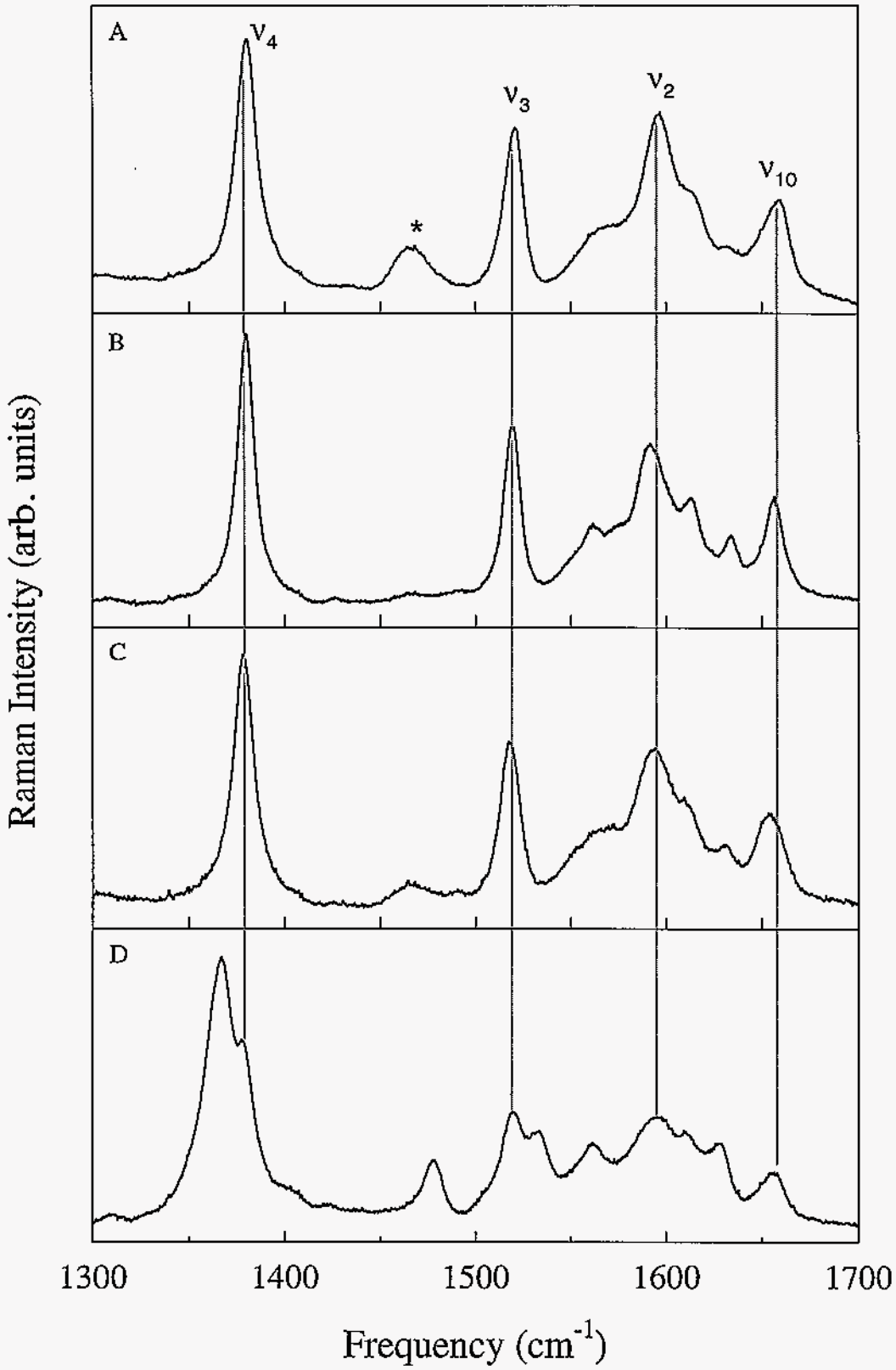
A
B
C
D
ν_4
ν_3
ν_2
ν_{10}
*
Raman Intensity (arb. units)
1300
1400
1500
1600
1700
Frequency (cm^{-1})

Figure 2.

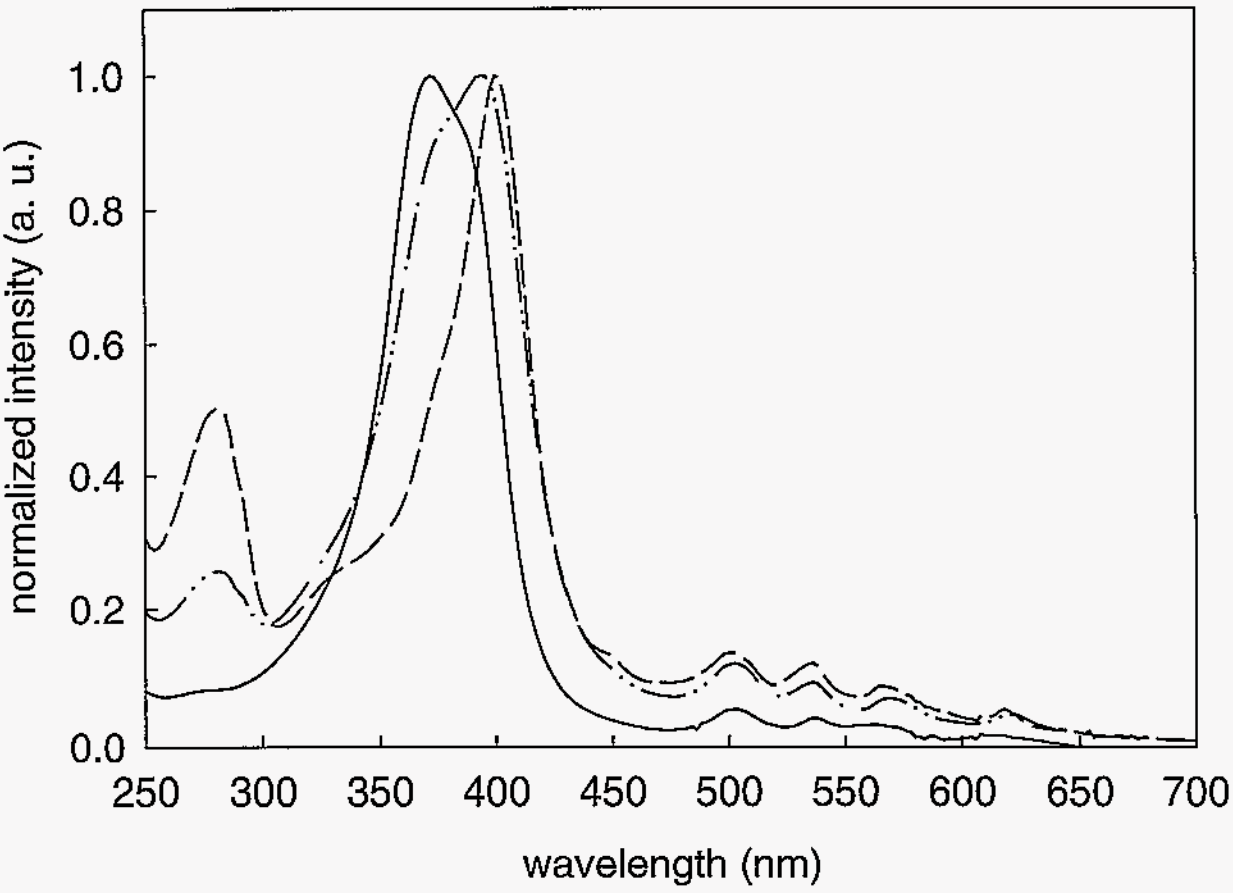
normalized intensity (a. u.)
1.0
0.8
0.6
0.4
0.2
0.0
250
300
350
400
450
500
550
600
650
700
wavelength (nm)

Figure 3.

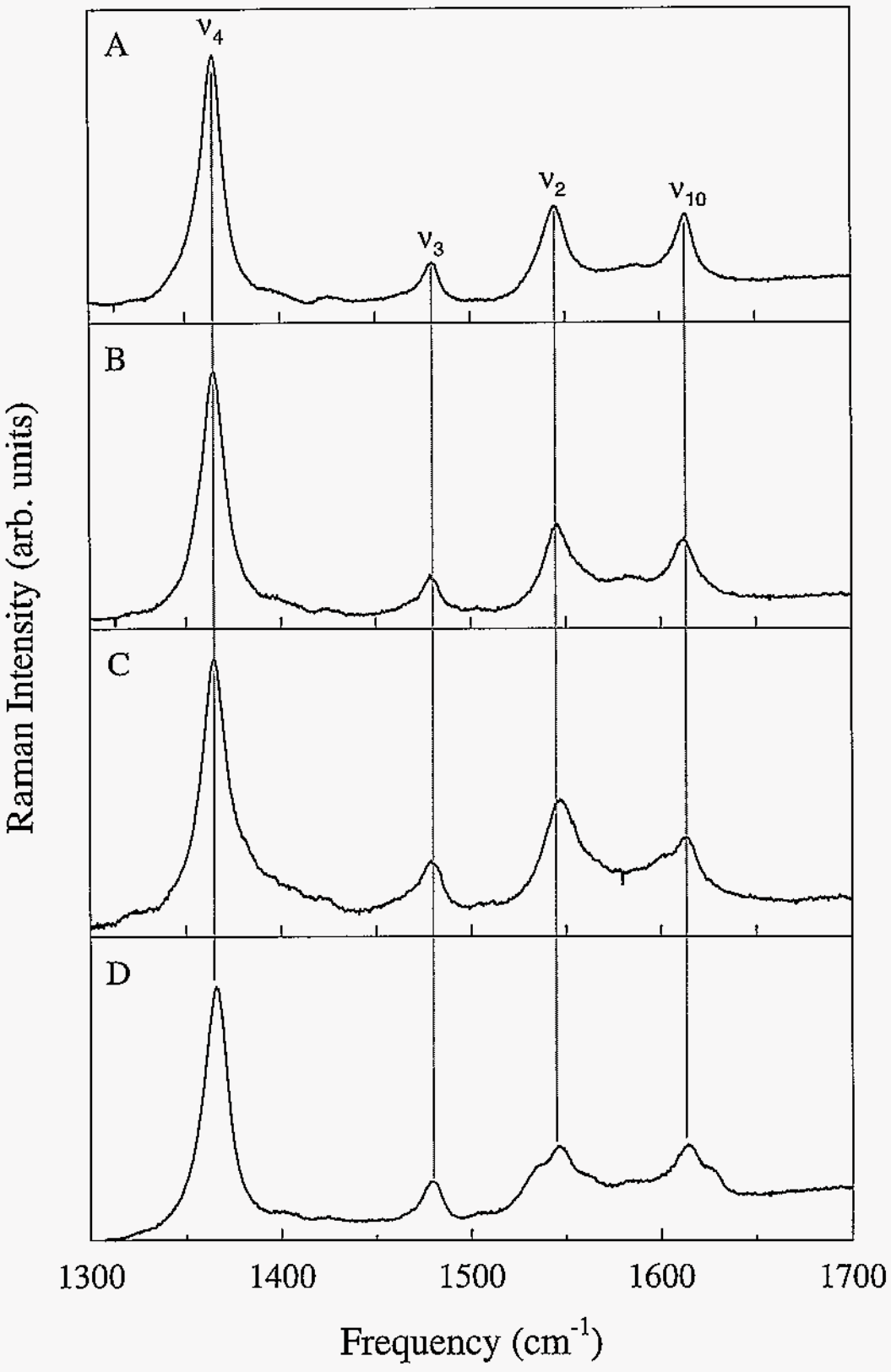
A
B
C
D
ν_4
ν_3
ν_2
ν_{10}
Raman Intensity (arb. units)
1300
1400
1500
1600
1700
Frequency (cm^{-1})

Figure 4.

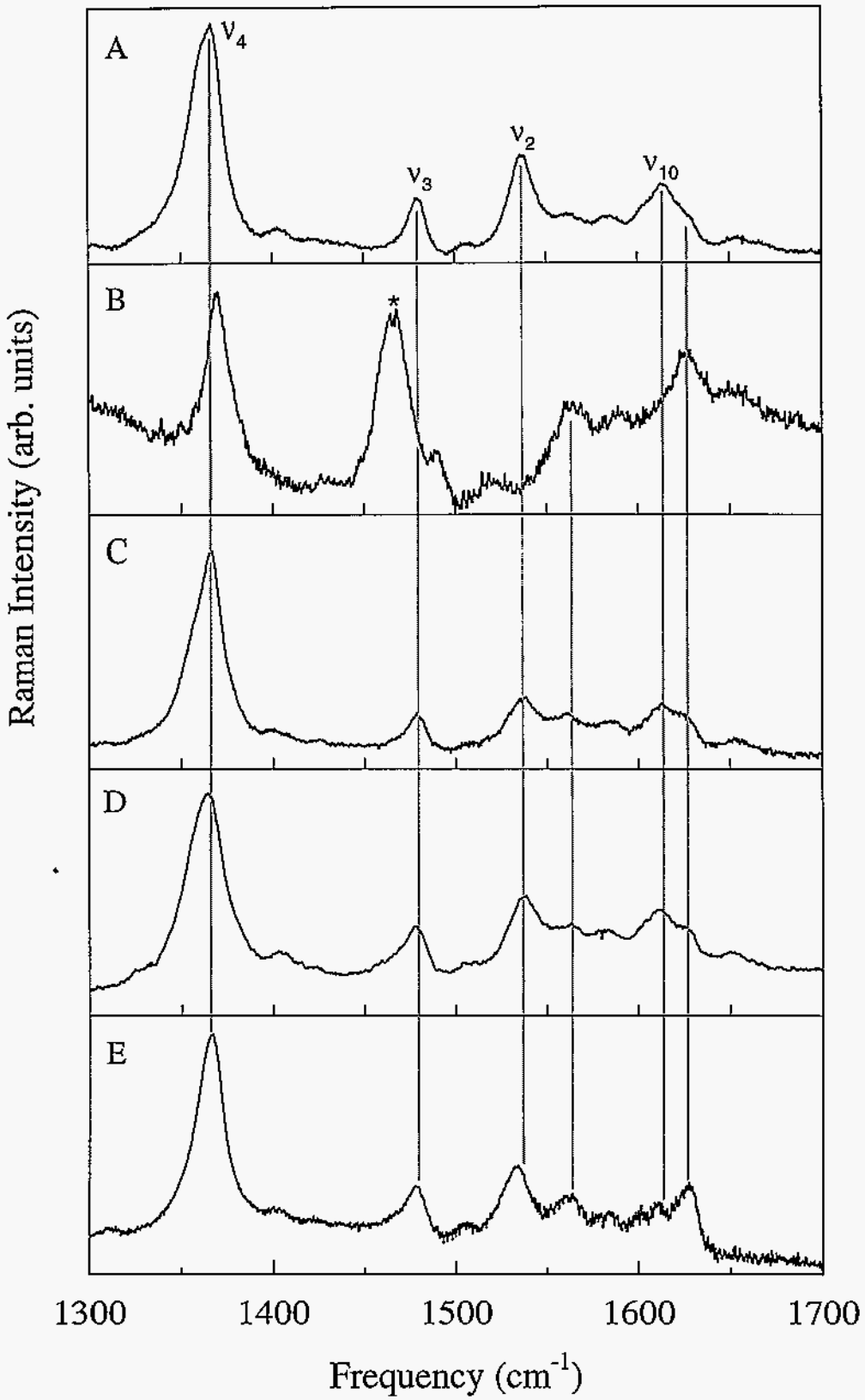
A
B
C
D
E
ν_4
ν_3
ν_2
ν_{10}
*
Raman Intensity (arb. units)
1300
1400
1500
1600
1700
Frequency (cm^{-1})

Figure 5.

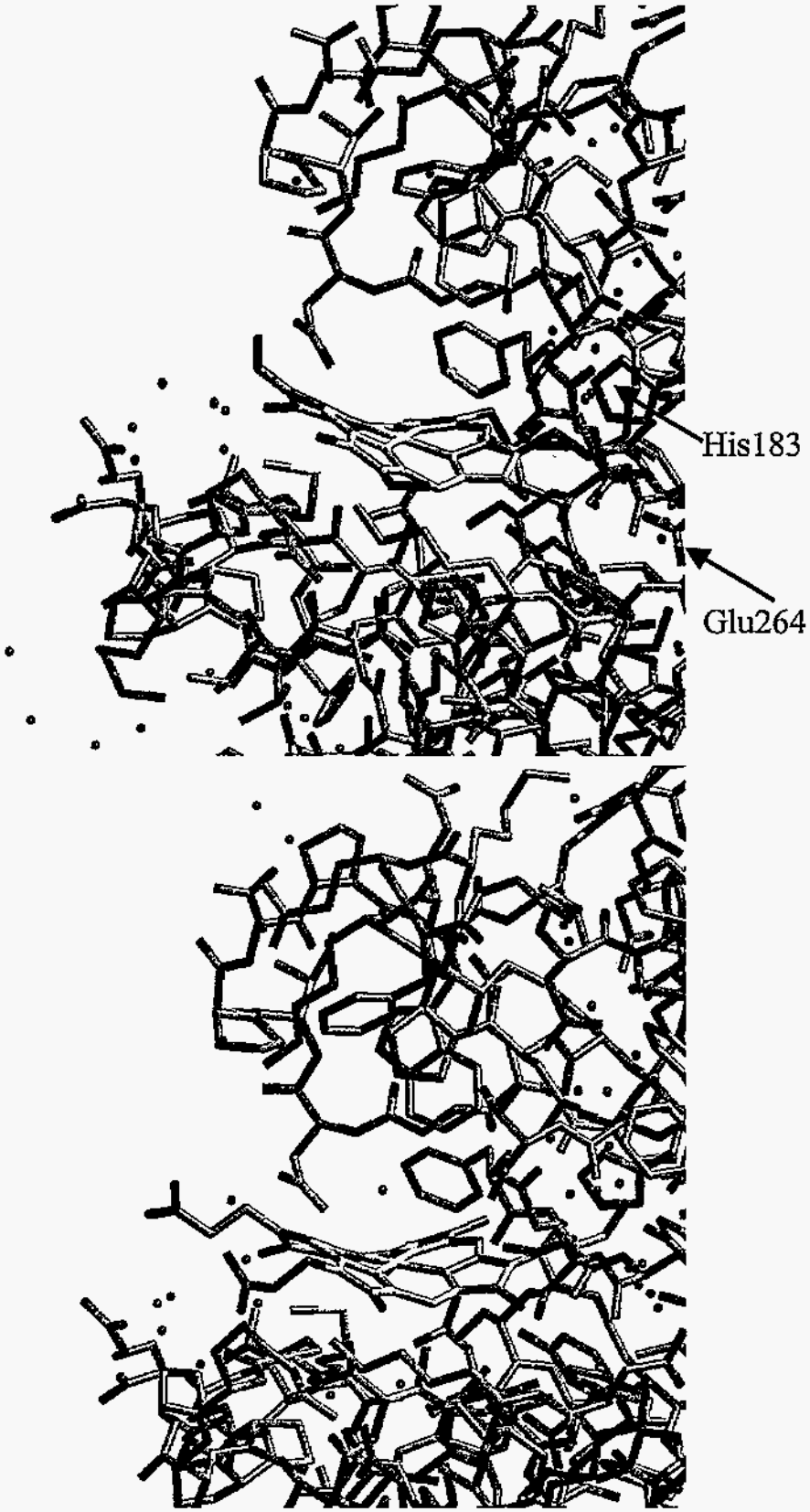

Figure 6.

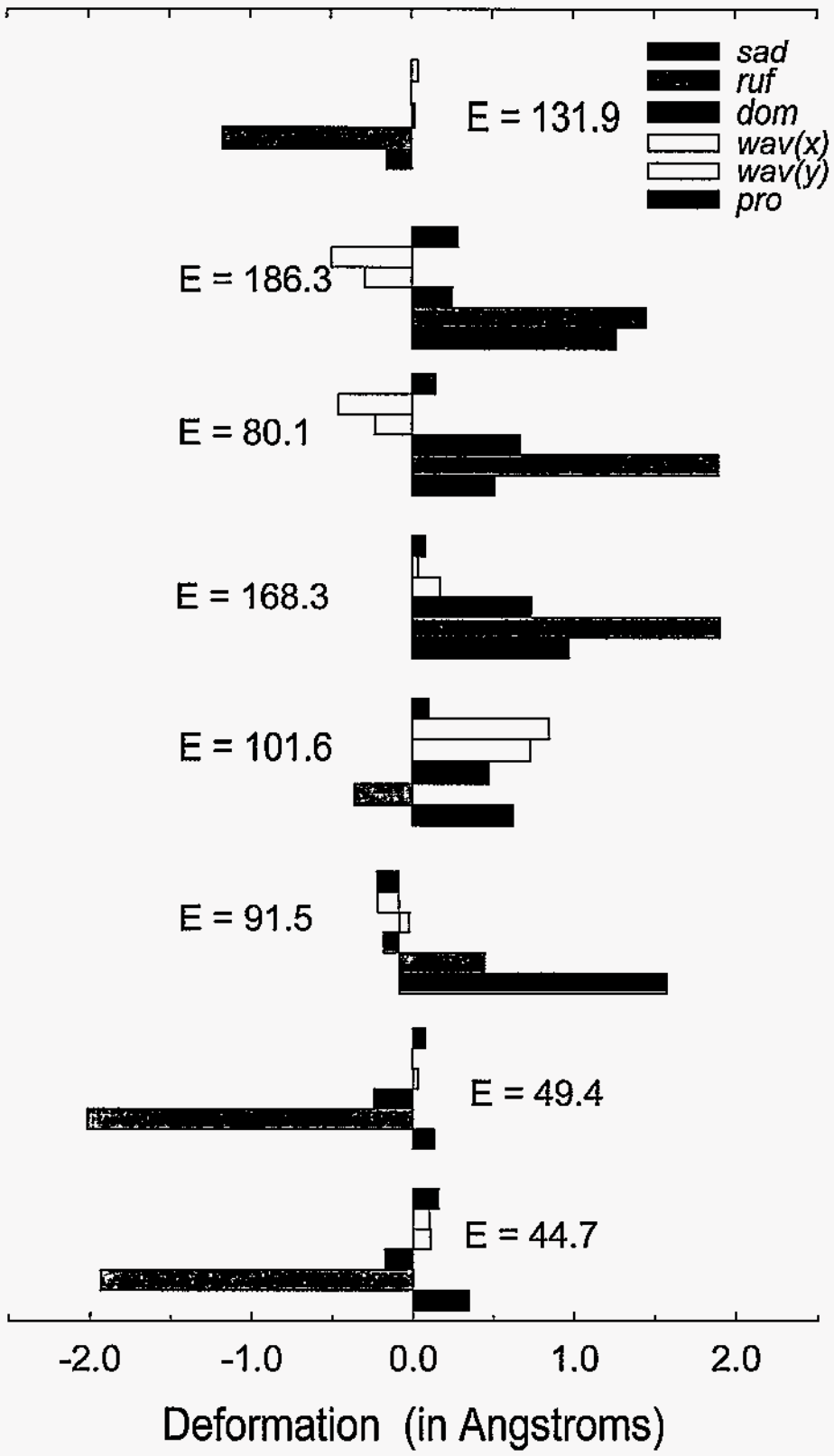
sad
ruf
dom
wav(x)
wav(y)
pro
E = 131.9
E = 186.3
E = 80.1
E = 168.3
E = 101.6
E = 91.5
E = 49.4
E = 44.7
-2.0
-1.0
0.0
1.0
2.0
Deformation (in Angstroms)

Figure 7.

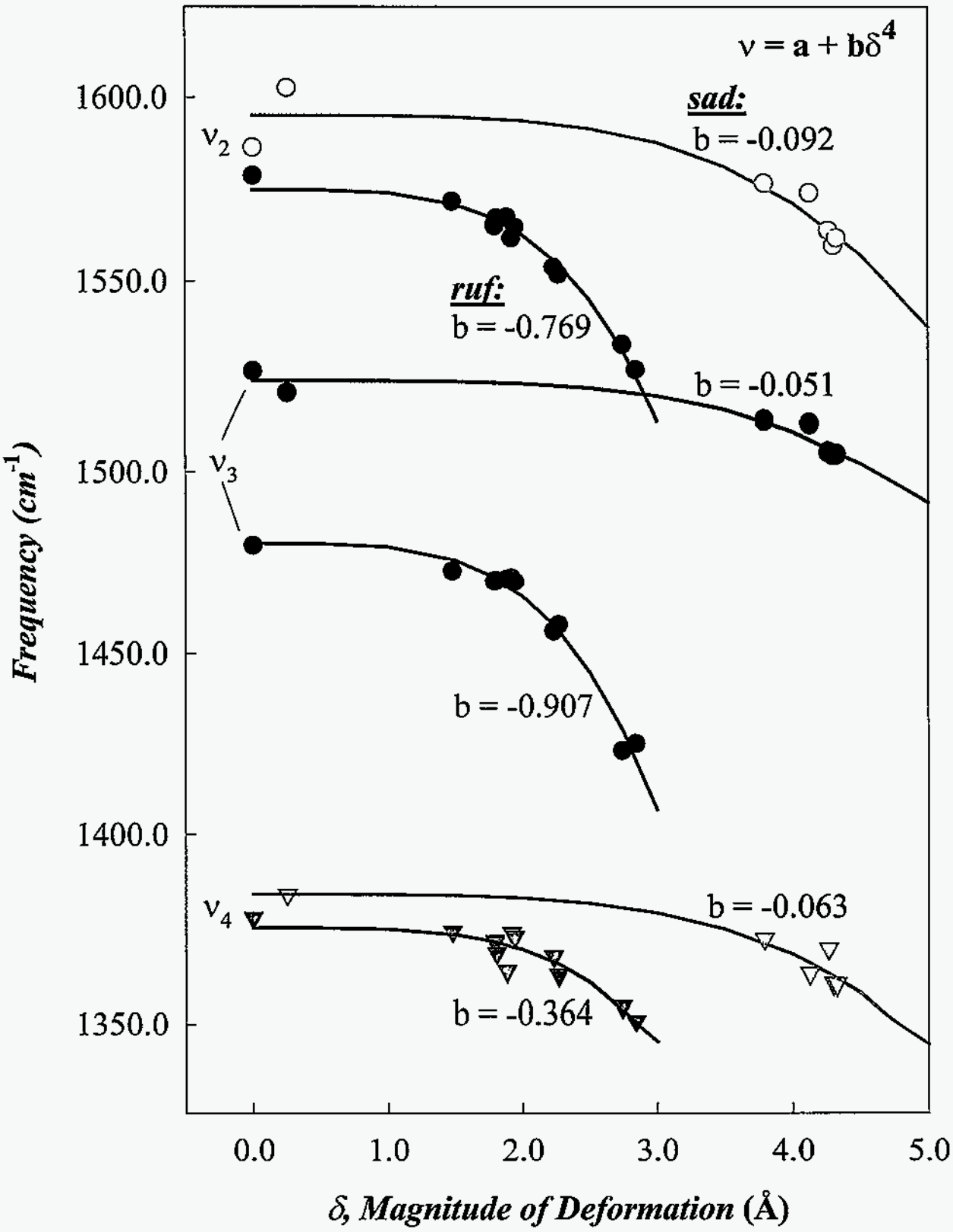
$\nu = a + b\delta^4$
sad:
b = -0.092
ruf:
b = -0.769
b = -0.051
b = -0.907
b = -0.063
b = -0.364
ν_2
ν_3
ν_4
1600.0
1550.0
1500.0
1450.0
1400.0
1350.0
0.0
1.0
2.0
3.0
4.0
5.0
Frequency (cm^{-1})
δ, Magnitude of Deformation (Å)

Figure 8.